

In vivo quantitative photoacoustic microscopy of gold nanostar kinetics in mouse organs

Weitao Li,^{1,2} Xiaolian Sun,² Yu Wang,² Gang Niu,² Xiaoyuan Chen,² Zhiyu Qian,^{1,4} and Liming Nie^{2,3,*}

¹Department of Biomedical Engineering, College of Automation Engineering, Nanjing University of Aeronautics and Astronautics, 29 Yudao Street, Nanjing, Jiangsu, 210016, China

²Laboratory of Molecular Imaging and Nanomedicine (LOMIN), National Institute of Biomedical Imaging and Bioengineering (NIBIB), National Institutes of Health (NIH), Bethesda, MD 20892, USA

³Center for Molecular Imaging and Translational Medicine, State Key Laboratory of Molecular Vaccinology and Molecular Diagnostics, School of Public Health, Xiamen University, Xiamen, 361005, China
⁴zhiyu@nuaa.edu.cn

* liming.nie@nih.gov

Abstract: We developed a high-resolution photoacoustic microscopy (PAM) system with a near-infrared (NIR) laser to noninvasively monitor the distribution of gold nanostar (GNS) in blood vessels, liver and spleen in mice. Photoacoustic images of organs at deep depths were continuously acquired *in vivo* every 30 minutes after a single dose of GNS by tail vein injection. The experimental results showed that GNS accumulated significantly in both liver and spleen from blood circulation after administration, which was qualitatively validated by fluorescence imaging. Our studies demonstrate that PAM might be potentially used for noninvasive tracing the kinetics of exogenous nanoparticles in biological system.

©2014 Optical Society of America

OCIS codes: (180.0180) Microscopy; (110.5125) Photoacoustics; (000.1430) Biology and medicine; (170.3880) Medical and biological imaging.

References and links

1. P. C. Li, C. W. Wei, C.-K. Liao, C.-D. Chen, K.-C. Pao, C.-R. Wang, Y.-N. Wu, and D.-B. Shieh, "Photoacoustic imaging of multiple targets using gold nanorods," *IEEE Trans. Ultrason. Ferroelectr. Freq. Control* **54**(8), 1642–1647 (2007).
2. C. Kim, C. Favazza, and L. V. Wang, "In vivo photoacoustic tomography of chemicals: high-resolution functional and molecular optical imaging at new depths," *Chem. Rev.* **110**(5), 2756–2782 (2010).
3. S. K. Balasubramanian, J. Jittiwat, J. Manikandan, C.-N. Ong, L. E. Yu, and W. Y. Ong, "Biodistribution of gold nanoparticles and gene expression changes in the liver and spleen after intravenous administration in rats," *Biomaterials* **31**(8), 2034–2042 (2010).
4. H. Chen, A. Dorrigan, S. Saad, D. J. Hare, M. B. Cortie, and S. M. Valenzuela, "In vivo study of spherical gold nanoparticles: inflammatory effects and distribution in mice," *PLoS ONE* **8**(2), e58208 (2013).
5. C. Pérez-Campaña, V. Gómez-Vallejo, M. Puigivila, A. Martín, T. Calvo-Fernández, S. E. Moya, R. F. Ziolo, T. Reese, and J. Llop, "Biodistribution of different sized nanoparticles assessed by positron emission tomography: a general strategy for direct activation of metal oxide particles," *ACS Nano* **7**(4), 3498–3505 (2013).
6. C. H. Lee, S. H. Cheng, Y. J. Wang, Y. C. Chen, N. T. Chen, J. Souris, C. T. Chen, C. Y. Mou, C. S. Yang, and L. W. Lo, "Near-Infrared Mesoporous Silica Nanoparticles for Optical Imaging: Characterization and In Vivo Biodistribution," *Adv. Funct. Mater.* **19**(2), 215–222 (2009).
7. S. Ye, R. Yang, J. Xiong, K. K. Shung, Q. Zhou, C. Li, and Q. Ren, "Label-free imaging of zebrafish larvae in vivo by photoacoustic microscopy," *Biomed. Opt. Express* **3**(2), 360–365 (2012).
8. S. Hu, K. Maslov, and L. V. Wang, "Noninvasive label-free imaging of microhemodynamics by optical-resolution photoacoustic microscopy," *Opt. Express* **17**(9), 7688–7693 (2009).
9. L. Xi, C. Duan, H. Xie, and H. Jiang, "Miniature probe combining optical-resolution photoacoustic microscopy and optical coherence tomography for in vivo microcirculation study," *Appl. Opt.* **52**(9), 1928–1931 (2013).
10. L. Nie, X. Cai, K. Maslov, A. Garcia-Urbe, M. A. Anastasio, and L. V. Wang, "Photoacoustic tomography through a whole adult human skull with a photon recycler," *J. Biomed. Opt.* **17**(11), 110506 (2012).
11. L. Nie, Z. Guo, and L. V. Wang, "Photoacoustic tomography of monkey brain using virtual point ultrasonic transducers," *J. Biomed. Opt.* **16**(7), 076005 (2011).
12. K. H. Song and L. V. Wang, "Noninvasive photoacoustic imaging of the thoracic cavity and the kidney in small and large animals," *Med. Phys.* **35**(10), 4524–4529 (2008).

13. L. Nie, M. Chen, X. Sun, P. Rong, N. Zheng, and X. Chen, "Palladium nanosheets as highly stable and effective contrast agents for in vivo photoacoustic molecular imaging," *Nanoscale* **6**(3), 1271–1276 (2014).
14. L. Nie, S. Wang, X. Wang, P. Rong, G. Niu, P. Huang, G. Lu, and X. Chen, "Plasmonic nanostars: in vivo volumetric photoacoustic molecular angiography and therapeutic monitoring with targeted plasmonic nanostars," *Small* **10**(8), 1585–1593 (2014).
15. K. H. Song and L. V. Wang, "Deep reflection-mode photoacoustic imaging of biological tissue," *J. Biomed. Opt.* **12**(6), 060503 (2007).
16. J. Yao and L. V. Wang, "Photoacoustic Microscopy," *Laser Photon Rev* **7**(5), 758–778 (2013).
17. H. Yuan, C. G. Khoury, H. Hwang, C. M. Wilson, G. A. Grant, and T. Vo-Dinh, "Gold nanostars: surfactant-free synthesis, 3D modelling, and two-photon photoluminescence imaging," *Nanotechnology* **23**(7), 075102 (2012).
18. S. Wang, P. Huang, L. Nie, R. Xing, D. Liu, Z. Wang, J. Lin, S. Chen, G. Niu, G. Lu, and X. Chen, "Single Continuous Wave Laser Induced Photodynamic/Plasmonic Photothermal Therapy Using Photosensitizer-Functionalized Gold Nanostars," *Adv. Mater.* **25**(22), 3055–3061 (2013).
19. J. Laufer, D. Delpy, C. Elwell, and P. Beard, "Quantitative spatially resolved measurement of tissue chromophore concentrations using photoacoustic spectroscopy: application to the measurement of blood oxygenation and haemoglobin concentration," *Phys. Med. Biol.* **52**(1), 141–168 (2007).
20. E. P. Visser, J. A. Disselhorst, M. Brom, P. Laverman, M. Gotthardt, W. J. G. Oyen, and O. C. Boerman, "Spatial resolution and sensitivity of the Inveon small-animal PET scanner," *J. Nucl. Med.* **50**(1), 139–147 (2008).
21. A. Chatzioannou, Y. C. Tai, N. Doshi, and S. R. Cherry, "Detector development for microPET II: a 1 μ l resolution PET scanner for small animal imaging," *Phys. Med. Biol.* **46**(11), 2899–2910 (2001).

1. Introduction

Exogenous nanomaterials such as gold nanoparticles (rods, cages, stars *etc.*), carbon nanotubes, and organic dyes are widely used in molecular imaging, tumor therapy, chemical and biological sensing, targeted diagnosis/therapy [1, 2]. Understanding the biodistribution and transport kinetics of nanoparticles (NPs) in biological systems is critically important for biological application and toxicity study. Various methods have been utilized to investigate metallic nanoparticles distribution in biological organs. For example, biodistribution of Au nanoparticle (NP) in liver, kidney and spleen were examined by inductively coupled plasma mass spectrometry (ICP-MS) analysis [3] or laser ablation inductively coupled plasma mass spectrometry (LA-ICP-MS) [4]. However, the above invasive methods require undesirable animal organ resection, which may bring ethical issues.

Positron emission tomography (PET) and fluorescence imaging are commonly available as noninvasive methods to monitor the biodistribution of nanoparticles in mice [5, 6]. However, both PET and fluorescence imaging usually require probe labeling and moreover are low in spatial resolution. Photoacoustic microscopy (PAM) is an emerging imaging modality that combines both rich optical absorption and high ultrasonic resolution in a single imaging modality [7–9]. Under irradiation of non-ionizing laser pulses, biological tissue absorbs the laser energy and generates heat, resulting in transient thermoelastic expansion and subsequent wideband ultrasonic emission. The produced ultrasonic pressures can be captured by ultrasonic transducers to form photoacoustic (PA) images.

Recently, PAM of deep objects in biological tissues has been extensively explored since laser in NIR region enables deep tissue penetration. PA imaging of primate brain through intact thick skull (up to 1 centimeter) was demonstrated [10, 11]. Dark-field PAM was developed to acquire the images of the atrium and the kidney of rat and rabbit *in situ* [12]. PA imaging with hand-held transducer was also used to measure the accumulation of NPs on exercised mouse organs [13]. Despite the preliminary studies, it is still demanded to explore PAM of NPs distribution noninvasively and continuously. Gold nanostar (GNS), one of the most typical gold nanoparticles, has been successfully applied as enhancing agent in photothermal therapy and PA imaging [14].

In this report, we developed a custom-built PAM system (nanoPAM, Shanghai) to trace the GNS kinetics, which shared similar principles with previous literatures [15, 16]. To the best of our knowledge, this is the first time to apply PAM to monitor the NPs distribution in organs from blood stream *in vivo*. The vascular structure and the internal organs with dynamic changes were clearly imaged by our PAM system with a wavelength of 730 nm. PA signal ratio of the organ to blood vessel in a region-of-interest (ROI) was calculated to semiquantify the GNS transport kinetics. In parallel, fluorescence images of the mice at the

same time points were acquired to validate the PAM results. Our experimental results demonstrate that PAM can potentially provide a noninvasive and semiquantitative method for monitoring NPs kinetics in organs and other deep imaging applications.

2. Materials and methods

The PAM system is schematically described in Fig. 1. The excitation system is a tunable laser source (Surelite OPO Plus, Continuum) pumped by a Surelite Series Nd:YAG laser. The laser system has a 7 ns pulse duration and 20 Hz pulse repetition rate. The laser beam was reflected by two optical mirrors, and then passed through a conical lens (Thorlabs Inc.) to form a ring-shaped laser beam and a homemade optical condenser to focus light on the mouse skin. The maximum 730 nm light energy at the surface of the mouse was ~ 5 mJ/cm². A two-dimensional motorized stage (Edmund, Barrington, NJ) and a programmable motion controller (Dover DMM 0200, MA) were used to move the light spot and ultrasonic transducer simultaneously. A 10 MHz ultrasonic transducer (NDT V-315, Olympus) was used to acquire ultrasound signals. A photodiode (PD) was used to both calibrate the PA signal and trigger signal acquisition. The received PA signals were then amplified by an amplifier (Olympus 5072PR) and digitized by a 14-bit high-speed data acquisition (DAQ) card (Gage Razor CompuScope CSE 1422) at a sampling rate of 50 MHz. In this study, we used the maximum amplitude projection (MAP) images to display the results.

GNS was synthesized following a reported method from cetyltrimethylammonium bromide (CTAB) [17]. The localized surface plasmon resonance (LSPR) of GNS was tuned approximately at 730 nm by adjusting the concentration of AgNO₃. We obtained the PEGylated GNS (GNS-PEG) by combining Au-S bonds. GNS-PEG had a good stability and dispersion in some solutions, such as ultrapure water and phosphate buffered saline (PBS). Figure 2(a) shows the transmission electron microscopy (TEM) image of GNSs. It can be seen that the GNS was in star morphology and the particle size was 56 ± 4 nm. The UV-vis-NIR spectrum of GNS with an absorption peak of 730 nm is shown in Fig. 2(b), thus 730 nm laser sources was used to trace GNS distribution in mice.

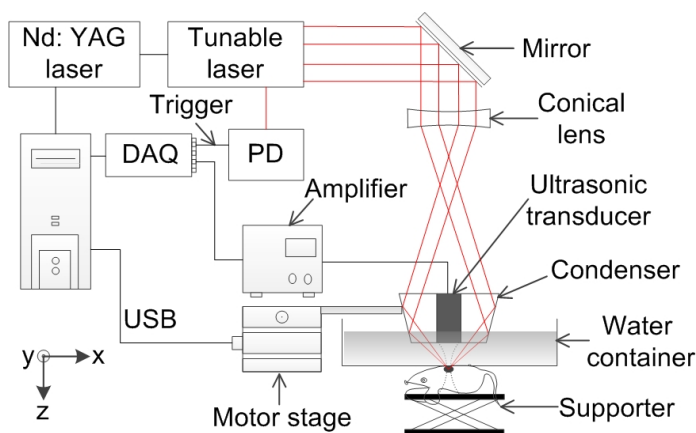


Fig. 1. Schematic of the PAM system for monitoring of NPs kinetics *in vivo*.

Conjugation of fluorescence probe, Cy5.5, to the GNS was performed by modifying a reported procedure [18]. Briefly, 10 mg HS-PEG-NH₂ was mixed with 10 mg GNS in water and was kept under shake at room temperature for 2 h. The prepared solution was centrifuged at 5000 relative centrifugal force (rcf) for 15 min and decanted to remove excess HS-PEG-NH₂. After three times centrifugation, the pellets were suspended in water. Then 3 mg NHS-Cy5.5 was dissolved in DMSO and gradually added into the above water solution. The mixture was shook at room temperature overnight. After that, the solution was centrifuged, decanted and suspended in ultrapure water and further purified using a dialysis bag (MWCO = 100k, Spectrum Laboratories, Inc).

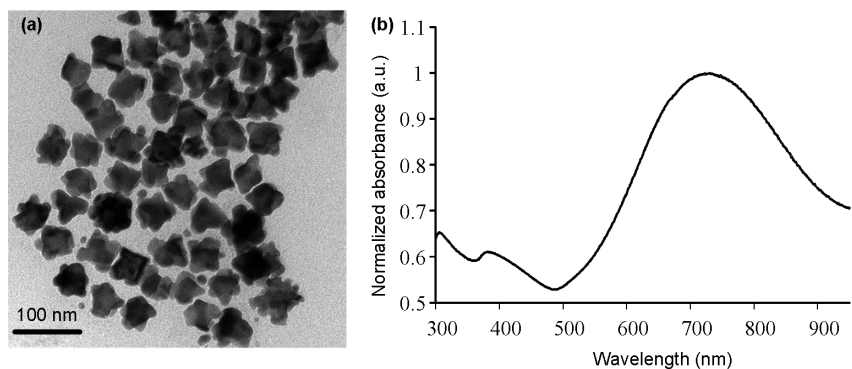


Fig. 2. (a) TEM image of GNS. The nanoparticle size is 56 ± 4 nm. (b) Absorption spectrum of GNS in water solution.

Immunodeficient nude mice weighting ~ 23 g were used for *in vivo* study. During experiment, the mice were maintained under anesthesia with a vaporized-isoflurane system (1L/min oxygen and 0.75% isoflurane, USP, Baxter Corp.) via a breathing mask. The body temperature of mice was kept by a water heating pad at 38°C . The mice were positioned on the supporter underneath the plastic membrane. Ultrasound gel (Parker Laboratories, Inc.) was pasted on the surface of the skin for acoustic coupling. GNS solution ($200\ \mu\text{L}$, $120\ \text{nM}$) was injected intravenously (i.v.) to the mice. Post-injection PAM scans on the organ area were performed at 7, 30, 60, 90, 120, 150, 180 min, respectively.

The fluorescence images were acquired using a commercial *in vivo* fluorescence imaging system (Maestro, Cambridge Research & Instrumentation Inc., MA). The fluorescence spectrum of Cy5.5 was firstly imported to the system library. The wavelength range of the excitation light source was from 640 nm to 820 nm with interval of 10 nm and the emission fluorescent signal was recorded at 702 nm. Illumination settings such as light energy and exposure time were automatically determined by the system. The fluorescence intensity was normalized to photons per second per centimeter square. Acquired fluorescence images were displayed and processed by Maestro software (Version 2.10.0). The average light intensity in the ROI was calculated and drawn via different time points. All animal handling was in accordance with the guidelines of Animal Committee of National Institutes of Health.

3. Results

The sagittal PA MAP image of a liver area was shown in Fig. 3(a). A section of the liver and its surrounding blood vessels were clearly imaged as marked by arrows. The liver in the PA image had an excellent match with the photograph of the live in Fig. 3(b) taken after the experiment. A B-scan image along the dotted line from Fig. 3(a) was shown in Fig. 3(c). To examine the imaging depth, a needle with a diameter of 0.5 mm and length ~ 1.5 cm was pierced into a mouse liver from the skin. A B-scan image displayed in Fig. 3(c) was acquired along the white dotted line in Fig. 3(a). The blood vessels were located between the skin and the liver. The B-scan image shows that the needle is obviously imaged with high contrast as marked by arrow. The results indicate that the imaging depth can reach as deep as ~ 4 mm from the mouse skin surface with a signal-to-background ratio of $>3:1$.

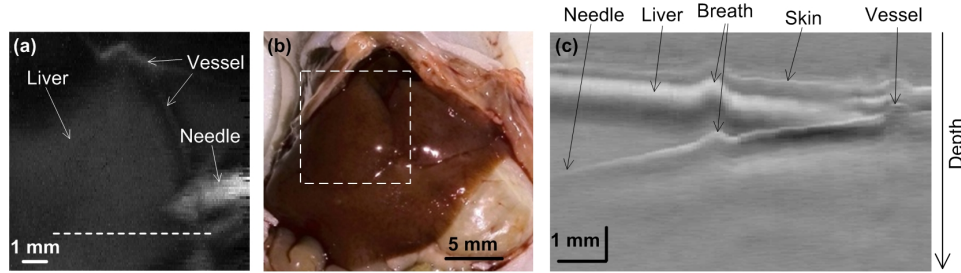


Fig. 3. (a) Sagittal PA MAP image of the liver corresponding to the dashed area in (b). (b) Anatomical photograph of the mouse liver with the skin removed after experiment. White dashed area indicates imaging area. (c) Axial B-scan PA image corresponding to the dotted line in (a) showing the imaging depth of the anatomical structure and needle.

To trace the GNS kinetics, PAM images of the liver and the spleen were continuously acquired in a mouse model. PAM imaging were performed right after i.v. injection of GNS shown in Fig. 4(a). The vasculature (first image in Fig. 4(a)) between skin and liver right after injection (7 min) had a higher PA signal than those in later images, indicating quick circulation of the GNS in blood vessels. After 0.5 h, the PA signal of liver tended to increase whereas the PA signal of vasculature began to decrease, which suggest the GNS accumulation to the liver from blood stream. In particular, the vasculatures at 3 h after injection were barely visible with low contrast because most GNS NPs were uptaken by the liver. For comparison, PAM imaging of another mice group were conducted as control at 7 min, 1, 2, 3 h after injection of 200 μ L of PBS. As can be seen in Fig. 4(b), PA signals of both blood vessel and liver in the control group were similar at different points.

In order to semiquantify the PA signal change, an identical ROI within a 2 mm \times 2 mm square on the liver (white dashed square in the first image of Fig. 4(a)) was selected in each PA image. The average PA signal in the ROI indicated by red arrow was divided by the PA signal in the blood vessel as indicated by white arrow at each time point. Then the calculated ratio was self-normalized to the first ratio in each group and the curve trend was illustrated in Fig. 4(c). The PA signal ratio of liver to blood vessel remarkably increased in the first hour, which indicated high accumulation of GNS. After 3 h, the ratio was approximately 8.5 times greater than that in the beginning. The semiquantitative imaging results suggest that PAM can clearly image the vessels and liver and monitor the transport kinetics of GNS.

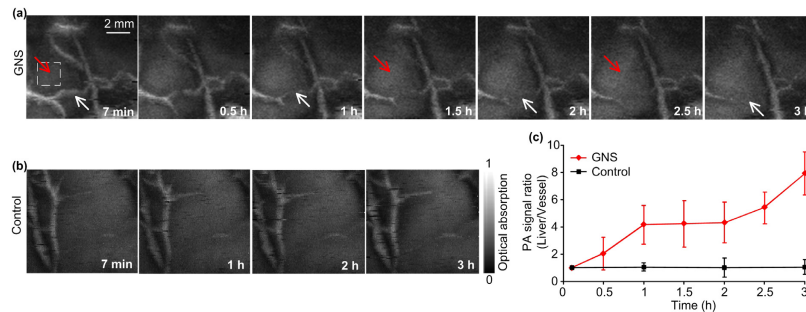


Fig. 4. PA MAP images and signal ratio change in the liver. (a) Sequential PA MAP images captured at 7 min, 0.5 h, 1 h, 1.5 h, 2 h, 2.5 h, and 3 h post-injection of GNS. Blood vessel and liver were indicated by white and red arrows, respectively. (b) Sequential PA MAP images obtained at 7 min, 1 h, 2 h, and 3 h post-injection of PBS as control. (c) Normalized PA signal ratio of liver to blood vessel curves derived from PA MAP images in (a) and (b), respectively. Values represent means \pm SD (n = 5/group).

Noninvasive PAM of spleen in mouse was conducted similarly to the PAM experiment of liver. The sequential PA MAP images of the adjacent region of the spleen represent the process of gradual accumulation of GNS to the spleen (Fig. 5(a)). The images show that the vasculature on the spleen right after injection (7 min) had a higher PA signal than those in

later images. After 7 min, the PA signal of spleen began to increase while the PA signal of vasculature decreased gradually, which suggest the GNS perfusion to the spleen from blood stream. For comparison, PA MAP images of mice injected by 200 μ L PBS were investigated at 7 min, 1, 2, 3 h as control group (Fig. 5(b)). Figure 5(a) shows that the vascular signals significantly decreased with increased PA signal in spleen, whereas the images in Fig. 5(b) remained almost unchanged.

The average PA signal in a ROI of spleen (2 mm \times 2 mm square in the dashed square) indicated by red arrow was divided by the PA signal in the blood vessel indicated by white arrow to semiquantify the signal change against different time points in Fig. 5(c). It was noted that the signal ratio remarkably increased in the first 1.5 h and then reached a plateau gradually. The ratio value at 3 h was approximately two times greater than that right after injection (7 min). The variations of GNS accumulation to liver and spleen could be influenced by NP size, morphology, surface modifications, observation time *etc.*

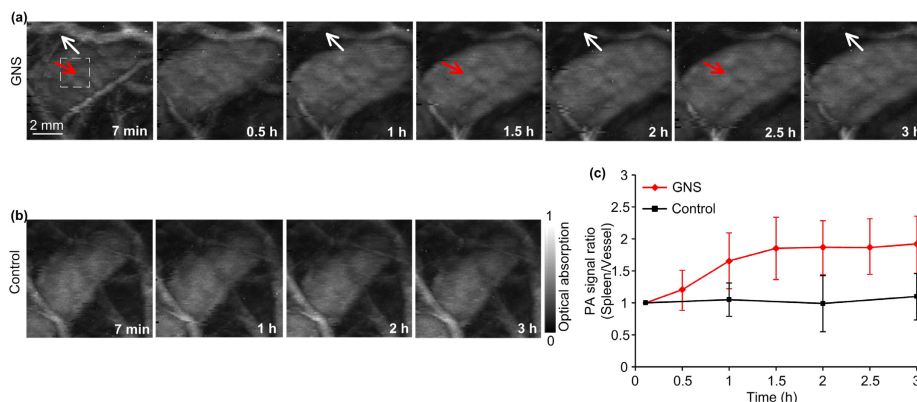


Fig. 5. PA MAP images and signal ratio change in a ROI of mouse spleen. (a) Sequential MAP images captured 7 min, 0.5 h, 1 h, 1.5 h, 2 h, 2.5 h, and 3 h post-injection of GNS. Blood vessel and spleen were indicated by white and red arrows, respectively. (b) Sequential MAP images achieved at 7 min, 1, 2, and 3 h post-injection of 200 μ L PBS. (c) PA signal ratio of spleen to blood vessel derived from PA MAP images in (a) and (b), respectively. Values represent means \pm standard deviation ($n = 5$ /group).

To further confirm the biodistribution results obtained from PAM, *in vivo* fluorescence images were collected and analyzed. GNS was labeled with NIR fluorescence probe (Cy5.5) for *in vivo* fluorescence imaging as described above. Figure 6(a) exhibits the series of the fluorescence images at different time intervals to show the dynamic distribution of GNS in the mouse. Although the boundaries of the organs were not well differentiated as shown in Fig. 6(a), stronger fluorescence signal was observed in the liver (indicated by red arrow) than that in the spleen (indicated by black arrow). PA signals come from not only the GNS but also the background absorbers such as hemoglobin and skin, *etc.* In contrast, fluorescence signals are dominantly contributed by Cy5.5 only. Since blood vessels are invisible in fluorescence imaging, only average fluorescent signals in the liver and the spleen were provided and plotted in Figs. 6(b) and 6(c), respectively. The fluorescent signal intensity in the liver region surged remarkably at the first half hour and then slowly afterwards. For the spleen, the signal intensity increased obviously at the first hour and then slowed down till 3 h. The fluorescence imaging results confirmed that the GNS prominently accumulated in the liver and the spleen after the circulation and more GNS are uptaken in liver than spleen. The slight variations between fluorescence imaging and PAM results are attributable to different imaging mechanisms of the two modalities.

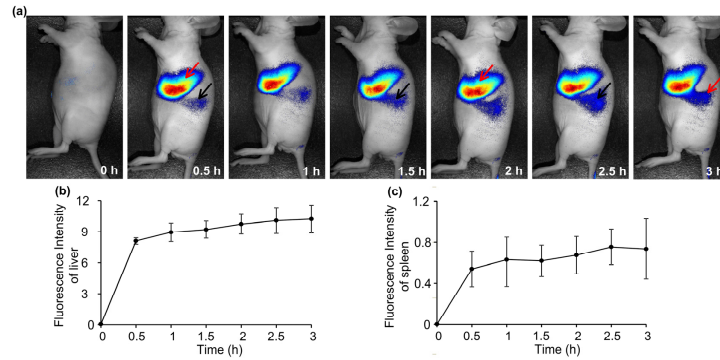


Fig. 6. Fluorescence images of the biodistribution of GNS-Cy5.5 in the liver (red arrow) and the spleen (black arrow). (a) *In vivo* fluorescence images of liver and spleen in mouse acquired before (0 h) and after injection (0.5, 1, 1.5, 2, 2.5, 3 h) of GNS-Cy5.5. (b) Average light intensity of the liver time-activity curve. (d) Average signal of the spleen time-activity curve. Fluorescence signal unit: 10^9 photons/cm²/s.

4. Conclusions and discussions

In summary, we successfully imaged and quantified the biodistribution of GNS in mouse liver and spleen. Dynamic tracing of GNS from the blood stream to organs was demonstrated by our PAM system. Since PA signal intensity is proportional to the concentration and absorption coefficient of nanoparticles [19], this proof-of-concept method can be extended to detect and monitor other types of nanoparticles (such as carbon nanotubes, gold nanorods and organic dyes) *in vivo*. The detecting depth of the current system is approximately 4 mm from the surface of the skin. By employing higher laser energy and longer laser wavelength, the imaging depth can reach even deeper. In addition to deep organ imaging, the method can detect the light absorption of NP kinetics directly and without dye labeling as required by fluorescence imaging. Compared with ICP, the proposed PAM method is noninvasive and capable of continuous monitoring. In this study, the PAM system only employs one ultrasonic transducer and the pulse repetition rate of the laser source is 20 Hz. In the future, we will employ ultrasound array transducer and a high pulse-repetition-rate laser source to improve the DAQ time.

Since most gold nanoparticles are non-fluorescent, fluorescence probes (Cy5.5 in this study) should be conjugated to GNS for fluorescence imaging. However, PAM can trace the GNS distribution directly without undesirable probe labeling. Moreover, PAM offers orders of magnitude higher resolution than fluorescence imaging because PAM converts photons into ultrasound pressures that are much less scattering in soft tissue. The resolution of AR-PAM system is determined by the central frequency and the numerical aperture (NA) of the ultrasonic detector. In our setup, the spatial resolution is approximately 100 μ m for 10 MHz transducer. However, the spatial resolution of state-of-the-art PET is only in millimeters, which is mainly determined by the detector size [20, 21]. In addition, PAM can monitor the circulation kinetics of GNS in blood vessels, which cannot be accomplished by the fluorescence instrument.

Acknowledgments

This work was supported by National Intramural Research Program (IRP) of the National Institute of Biomedical Imaging and Bioengineering (NIBIB), NIH, and National Natural Science Foundation of China (61275199, 81301257, and 61378092), National Key Basic Research Program (973 project) (2014CB744503), as well as the NUAA Fundamental Research Funds (NS2013035). The authors acknowledge instrumental and technical support from nanoPAM, United Well Inc. We also thank Mr. Darius Zamani for close reading of the manuscript.